Phys. Status Solidi A **210,** No. 2, 395–402 (2013) / **DOI** 10.1002/pssa.201228498

physica status solidi a
www.pss-a.com
applications and materials science

Effect of conducting polymer layer on microwave absorption properties of $BaFe_{12}O_{19}$–TiO_2 composite

O. Akman[1,2], Z. Durmus[3], H. Kavas[4], B. Aktas[1], U. Kurtan[3], A. Baykal[3], and H. Sözeri[*,5]

[1] Physics Department, Gebze Institute of Technology (GYTE), 41400 Gebze-Kocaeli, Turkey
[2] Department of Physics, Sakarya University, 54100 Sakarya, Turkey
[3] Department of Chemistry, Fatih University, 34500 B. Cekmece-Istanbul, Turkey
[4] Department of Engineering Physics, Istanbul Medeniyet University, Istanbul 34720, Turkey
[5] TUBITAK-UME, National Metrology Institute, PO Box 54, 41470 Gebze-Kocaeli, Turkey

Received 24 July 2012, revised 1 October 2012, accepted 5 October 2012
Published online 2 November 2012

Keywords conducting polymers, hexaferrite, microwave absorption, nanocomposites, TiO_2

* Corresponding author: e-mail huseyin.sozeri@tubitak.gov.tr, Phone: +90 262 679 5000, Fax: +90 262 679 5001

Ba-hexaferrite (BaM) particles, synthesized by a sol–gel route, have been mixed with TiO_2 powders with different mass ratios. The obtained BaM–TiO_2 composites have been coated with a conducting polymer layer of polypyrrole (PPy). Structural, magnetic and microwave absorption properties of the PPy-coated and uncoated BaM–TiO_2 composites have been investigated by X-ray diffractometry (XRD), scanning/tunneling electron microscopy, magnetization, and near-field microwave measurements in the frequency range of 8–18 GHz. The dielectric loss of the PPy-coated composites appeared to be higher compared to the uncoated samples in the whole frequency range. A single matching frequency was observed for each of the coated and uncoated samples in the frequency range between 16 and 18 GHz. Despite their relatively low absorption properties of uncoated composites (∼−30 dB), PPy-coated ones have wide absorption bandwidths at −20 dB. The main absorption mechanism in all samples, coated and uncoated, is dielectric loss.

1 Introduction Microwave absorbers have been in use, both in civil and military applications, due to their ability to reduce electromagnetic interference (EMI) and to reduce radar signatures for a long time. EMI can be prevented either by reflecting the EM radiation or by absorbing it. The former can be achieved by materials having free charge carries, namely with conductors. However, the usage of metals as shielding materials is limited due to their heavy weight and corrosive nature. Carbon-based materials like single or multiwall carbon nanotubes, graphene and carbon black were also used as an alternative conducting material [1–4]. Their disadvantage is that synthesis in large amounts is difficult and costly. Besides, they need complicated purification and functionalization procedures [5, 6]. The second mechanism of EMI shielding, *i.e.*, absorption, can be achieved by the presence of dielectric and magnetic fillers that interact with electric- and magnetic-field components of the EM wave. As dielectric fillers TiO_2, ZnO, Al_2O_3, $BaTiO_3$ and magnetic fillers Ni, Co, Fe_3O_4, spinel, and hexaferrites have been used [7–10].

Recently, intrinsic conducting polymers (ICP) appear to be good candidates and have opened up new horizon in the field when they are used as an EMI shielding material due to the higher electrical conductivity, ease of processability, low density, good corrosion resistance. ICPs with dielectric and/or magnetic fillers combined the two shielding mechanism in a single material and have attracted significant attention in recent years [11, 12]. ICPs have only electrical loss, which is not solely enough to synthesize good absorbing materials. For this reason, magnetic fillers such as spinel and/or hexaferrites together with additional dielectric materials are generally needed. It is possible to control the electromagnetic properties of such composites by varying the chemical compositions and weight fractions of the fillers. In this way, saturation magnetization, magnetocrystalline anisotropy, permeability, and permittivity of the composite may change so that broadening of the absorption bandwidth or shift of the resonance frequency can occur. In addition to composition, crystal structure of the ferrites has an important

effect on the absorption properties. Ferrites with spinel structure, *e.g.*, can be used in the frequency range of several hundred MHz to a few GHz. One of the major problems of the soft magnetic absorbers is the rapid decrease of permeability, *i.e.*, magnetic loss, in the GHz range as given by Snoek's limit [13]. On the other hand, hexaferrites can be used in a wide frequency range up to ~50 GHz due to their high natural resonance frequency [14, 15]. For this reason, M-type hexagonal ferrites are a special kind of absorbers due to their magnetic and dielectric losses in the microwave band and have been extensively studied to prepare high-frequency absorbers. The resonance phenomena in ferrites can be explained by two different mechanisms: spin resonance and domain-wall motion [16]. For polycrystalline ferrite, the permeability spectrum can be described by the combination of both contributions. However, the complex permeability in the high-frequency region is generally affected by the spin rotation component [17].

Among ICPs, polyaniline (PANI) and polypyrrole (PPy) are the most extensively studied ones, mainly because of their unique doping mechanism and controllable conductivity with excellent physical and chemical properties including thermal stability [18, 19]. He et al. [20], *e.g.*, incorporated Fe_3O_4 nanoparticles into PANI by chemical oxidative polymerization and obtained ~−48 dB absorption at 9.6 GHz. Phang et al. [21] added dielectric filler, TiO_2, to the Fe_3O_4/PANI composite and observed that as TiO_2 concentration increases reflection loss (RL) decreases. On the other hand, with increasing Fe_3O_4 concentration RL also increases up to ~−25 dB. Barium hexaferrite, $BaFe_{12}O_{19}$, is extensively used as a magnetic filler in a conducting polymer matrix in the literature. Du et al. [22] doped $BaFe_{12}O_{19}$ with Co–Ti cations and used PANI as ICP to obtain RL of −35 dB with 2 mm thickness. Yang et al. [23] synthesized ($BaFe_{12}O_{19} + BaTiO_3$)/PANI composite by in situ polymerization. In this study, $BaFe_{12}O_{19} + BaTiO_3$ blend showed three absorption bands at 9.6, 31.0, and 38.2 GHz with −7.5, −12.0, and −33.0 dB in RL, respectively, while ($BaFe_{12}O_{19} + BaTiO_3$)/PANI composite exhibited three relatively pronounced absorption bands at 7.4, 22.0, and 36.0 GHz with RLs of −10.4, −18.0, and −22.0 dB, respectively. Akman et al. [24] prepared the Ni, Co, and Ni–Co alloyed coatings on polyacrylonitrile (PAN) fibers. They found that the composite prepared in a Ni bath for 0.5 min leads to a wider absorption bandwidth and minimum coefficient of reflection, about of −42 dB, more than 99.99% of the microwave absorption.

In this study, PPy was used as a conducting polymer and BaM ($BaFe_{12}O_{19}$) nanoparticles as a magnetic filler. TiO_2 powders, with different weight fractions, were used as a dielectric filler. The structural, electrical, magnetic, and microwave absorption properties of $BaFe_{12}O_{19}$–TiO_2–PPy composites have been studied by X-ray diffractometry (XRD), transmission electron microscopy (TEM), Fourier transform infrared (FT-IR), dc conductivity, vibrating sample magnetometry (VSM), and vector network analyzer (VNA) techniques. The microwave properties of these composites were compared with those having the same magnetic to dielectric weight fractions but without PPy coating.

2 Experimental

2.1 Chemicals and instrumentations All chemicals, barium nitrate ($Ba(NO_3)_2 \cdot 4H_2O$), ferric nitrate ($Fe(NO_3)_2 \cdot 4H_2O$), titanium oxide (TiO_2), HCl, PPy monomer, ammonium peroxy disulfate (APS) were obtained from Merck and were used as received, without further purification.

Structural and morphology of the samples were investigated by FT-IR, XRD, thermogravimetric analysis (TGA), and high-resolution transmission electron microscopy (HR-TEM).

The crystallite size and phase fractions of the samples were determined from the XRD patterns (Rigaku Smart Lab, Cu-K_α radiation).

FT-IR spectra were recorded in transmission mode with a Perkin Elmer BX FT-IR infrared spectrometer. The powder samples were ground with KBr and compressed into a pellet. FT-IR spectra in the range 4000–400 cm^{-1} were recorded in order to investigate the nature of the chemical bonds formed.

The thermal stability was determined by TGA (Perkin Elmer Instruments model, STA 6000). The TGA thermograms were recorded for 5 mg of powder sample at a heating rate of 10 °C min in the temperature range of 30–800 °C under nitrogen atmosphere. The magnetic characterization of the samples was performed at room temperature (RT) using a vibrating sample magnetometer (LDJ Electronics Inc., Model 9600) in an applied field of 15 kOe.

In order to make microwave measurements using a VNA, samples were pressed in the form of rectangular pellets with dimensions $10.2 \times 22.8\ mm^2$ for X-band and $15.8 \times 7.9\ mm^2$ for Ku-band with a thickness of 2 mm. Then, they are inserted into the copper holder, which is placed between two waveguides. The scattering parameters of samples for reflection (S11 or S22) and absorption (S12 or S21) were determined by an HP 8510C VNA. Full two-port calibration was performed to remove some errors due to the directivity, source match, load match, etc., in both forward and reverse directions. HR-TEM analysis was performed using a JEOL JEM 2100 microscope. A drop of diluted sample in alcohol was dripped on a TEM grid. Ball milling was performed with a Retsch "PM-400" planetary ball mill in tungsten carbide jars.

2.2 Synthesis The nanocomposites of $BaFe_{12}O_{19}$ and TiO_2 were prepared by a sol–gel method. The TiO_2 sol and $BaFe_{12}O_{19}$ sol were synthesized, respectively, first, TiO_2 was used after ball milling with Retsch "PM-400" planetary ball mill in tungsten carbide jars. Barium nitrate and ferric nitrate with a molar ratio of 1:12 were dissolved in 60 °C ethylene glycol with the addition of citric acid. After the ethylene diamine was added to adjust the pH value to 7.0, the $BaFe_{12}O_{19}$ precursor sol was formed. According to the concentration of TiO_2 for 0.7, 3.5, and 12.5 wt.%, three

Table 1 Sample codes and their magnetic ($BaFe_{12}O_{19}$) to dielectric (TiO_2) weight fractions.

sample code	PPy coating	$BaFe_{12}O_{19}$ weight fraction	TiO_2 weight fraction
A11	no	1/2	1/2
A12	no	1/3	2/3
A21	no	2/3	1/3
B11	yes	1/2	1/2
B12	yes	1/3	2/3
B21	yes	2/3	1/3

mixed sols were prepared. After being evaporated at 80 °C and calcined at 850 °C, the composites were finally obtained. PPy–$BaFe_{12}O_{19}$–TiO_2 nanocomposite was prepared by *in situ* polymerization of pyrrole. In a typical procedure, a certain amount of $BaFe_{12}O_{19}$–TiO_2 nanoparticles was added to 35 mL of 0.5 M HCl solution containing 1 mL of pyrrole monomer sonicated in an ultrasonic bath for 120 min at RT. Then 3.5 g of APS in 20 mL of 0.5 M HCl solution was slowly added dropwise to the above mixture. The polymerization was carried out in ultrasonic bath at RT. The composite was obtained by filtering and washing the reaction mixture with deionized water and ethanol and dried under vacuum at 50 °C for 24 h. $BaFe_{12}O_{19}$–TiO_2 nanocomposite was thus synthesized. Samples having different $BaFe_{12}O_{19}$:TiO_2 weight fractions with and without PPy layer were prepared and abbreviated as shown in Table 1.

3 Results and discussion

3.1 XRD analysis Figure 1 shows the X-ray diffraction pattern of pure BaM (Fig. 1a) and the sample B21 (Fig. 1b). All the observed peaks were matched with the standard XRD pattern of $BaFe_{12}O_{19}$ (JCPDS No. 84–0757) and additionally Fig. 1b was also matched with the standard XRD pattern of TiO_2 (JCPDS No. 99–100–4701). Figure 1a shows that single-phase BaM particles were obtained with the synthesis conditions mentioned before. The mean size of the crystallites was estimated from the diffraction pattern by line-profile fitting [25]. The line profile, shown in Fig. 1 was fitted for observed 22 peaks with the following Miller indices: (104), (106), (110), (008), (107), (114), (200), (108), (203), (116), (205), (206), (1011), (209), (300), (303), (1112), (218), (219), (220), (2111), and (2014). The average crystallite size of the pure BaM particles, D and σ, were 30 ± 10 nm. In Fig. 1b, peaks belonging to $BaFe_{12}O_{19}$ were observed in the sample B21, which designates the presence of ferrite particles in the polymer matrix. However, TiO_2 can hardly be observed probably due to its low concentration. The shoulder around $2\theta = 20$ is due to PPy in the matrix.

3.2 SEM/TEM analysis Figure 2 shows SEM micrographs of the Ba-hexaferrite NPs with different magnifications. It is observed that grains have rounded edges with

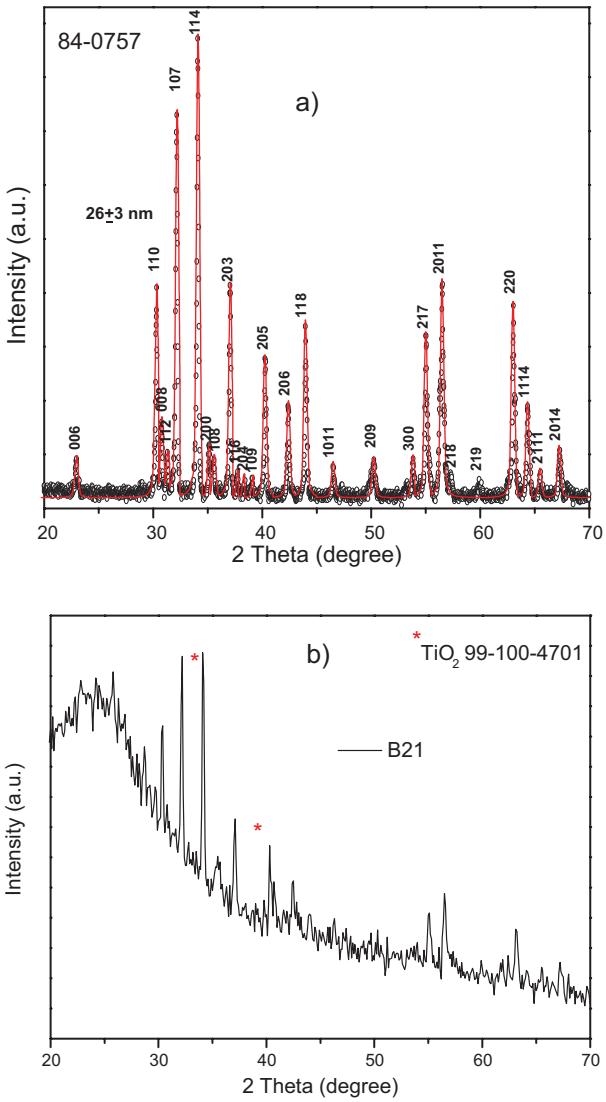

Figure 1 (online color at: www.pss-a.com) XRD powder patterns of (a) pure BaM and (b) PPy–BaM–TiO_2.

sizes between 200 and 600 nm as measured with the microscope ruler. This means that they are all within the single domain limit of 1 μm [26]. Intergrain connectivity seems to be weak probably due to the heat treatment at low temperature. Some agglomerations of different sizes and masses are present. Figure 2a shows an HR-TEM micrograph of Ba-hexaferrite crystallites that have broad size distribution from 20 to 80 nm. The presence of TiO_2 and Ba-hexaferrite nanoparticles is obvious in Fig. 2b. When these nanoparticles were coated with PPy, a continuous overlayer of conducting polymer is produced on the particles surface as seen in Fig. 2f. They also show agglomerated morphology. Figure 2f reveals that the BaM particles are platelets, and aggregated due to magnetic attraction between the particles. After coating with PPy, it is clearly seen that the continuous coverage of PPy has been produced on the

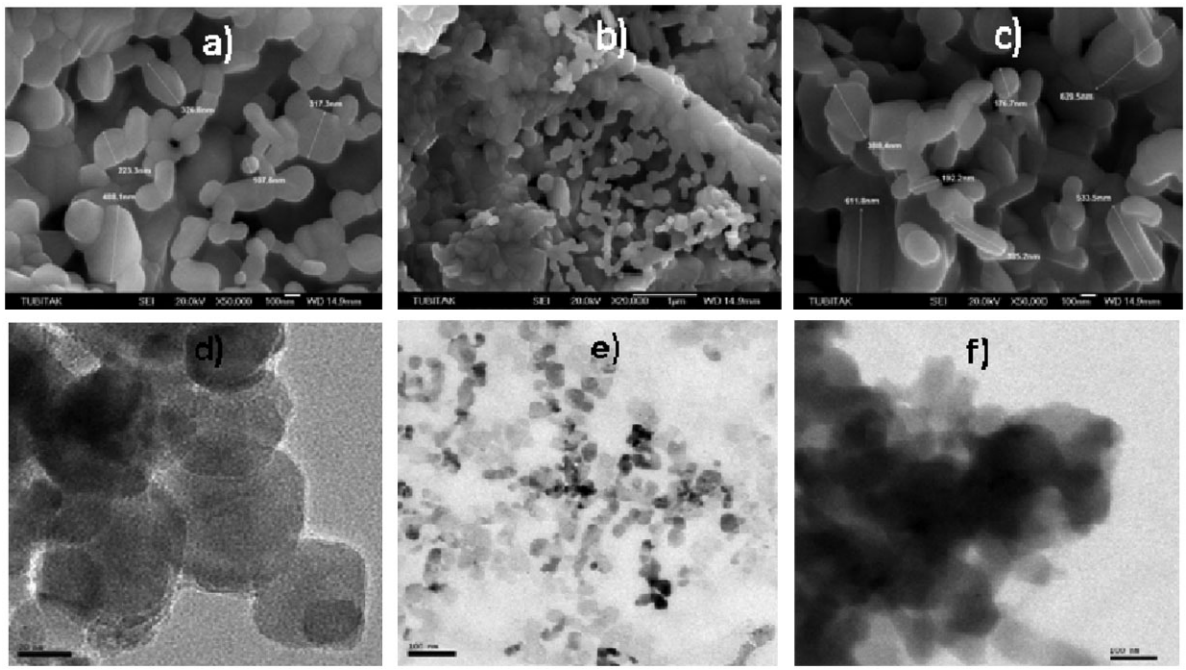

Figure 2 (a)–(c) SEM micrographs of pure $BaFe_{12}O_{19}$ powders, TEM micrographs of (d) $BaFe_{12}O_{19}$ crystallites, (e) BaM–TiO_2 composite, and (f) BaM–TiO_2–PPy composite.

platelet BaM surfaces in Fig. 1b. In comparison with the uncoated BaM particles, the PPy formed on the surface of M-Ba-ferrite particles leads to the increase of the particle size.

3.3 FT-IR analysis The FT-IR spectrum of the B21 nanocomposite clearly exhibits characteristic absorption peaks with respect to PPy in Fig. 3. The band at 1540 cm^{-1} corresponds to the C–C and C=C stretching vibrations and that at 1460 cm^{-1} reflects C–N stretching vibration. The bands of the C–H or C–N and the bands of the C–H and N–H inplane deformation vibrations are situated at 1290 and 1036 cm^{-1}, respectively [27].

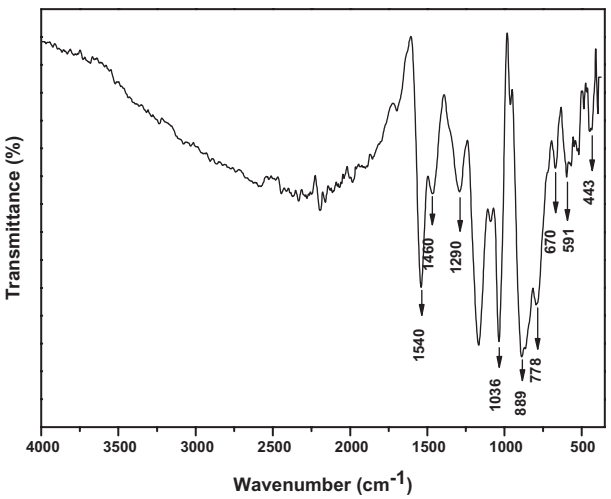

Figure 3 The FT-IR spectrum of the B21 nanocomposite.

The absorptions at 889, 778, and 670 cm^{-1} are related to the C–H outer-bending vibrations. These results indicate the formation of PPy in the composite. The characteristic peak for pure $BaFe_{12}O_{19}$ can be seen at around 591 and 443 cm^{-1} (correspond to vibrations of the tetrahedral and octahedral sites for $BaFe_{12}O_{19}$) [28–30].

3.4 TGA analysis Thermal gravimetric analysis was performed in order to investigate the stability and inorganic loading of the B11, B12, and B21 nanocomposites and the resultant thermograms are presented in Fig. 4. There is one significant weight loss around 100 °C due the evaporation of adsorbed water. Then, composites lose their masses rather steadily in the temperature range of 100–750 °C after which all of the organic part is removed. The total weight loss of ~55% occurs due to the decomposition of PPy in the composite. This means that nearly half of the total mass of the composites belongs to the conducting polymer and other half includes BaM–TiO_2 fillers [28].

3.5 Magnetization measurements Figure 5 shows RT *M–H* hysteresis curves of pure BaM and composites B11, B12, and B21. BaM particles have specific saturation magnetization (M_s) of nearly 60 emu g^{-1} at 15 kOe and quite high coercivity of 4.8 kOe, as seen in Fig. 5a. When these particles were mixed with dielectric ones, M_s decreases linearly with the weight fraction of the magnetic part. The TGA data presented in Fig. 4 shows that almost half of the

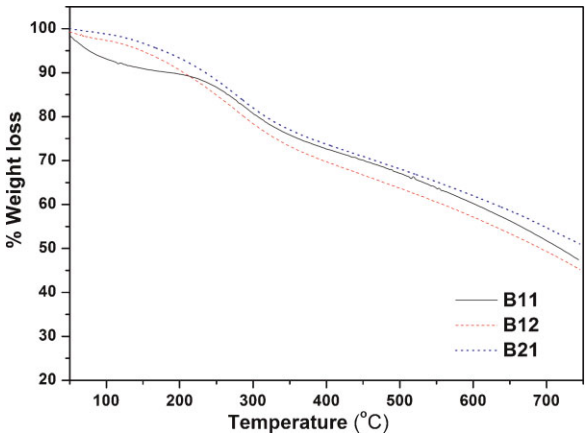

Figure 4 (online color at: www.pss-a.com) TGA curve of B11, B12, and B21 nanocomposites.

total mass of $BaFe_{12}O_{19}$–TiO_2–PPy nanocomposite belongs to the conducting polymer, PPy. This means that the mass fraction of the magnetic part decreases further, which leads to another decrease in M_s. It should be noted here that all the *M*–*H* hysteresis curves in Fig. 5b belong to the $BaFe_{12}O_{19}$–TiO_2 nanocomposites. In other words, the magnetization values in these curves are not normalized according to their magnetic weight fractions. They are presented here to compare their magnetizations per gram of composite. In addition to the decreasing mass fraction of magnetic filler, there is another reason that can diminish the magnetization of the composite. This is the adsorption of PPy molecules to the surface of $BaFe_{12}O_{19}$ NPs. During the coating process, some of the $BaFe_{12}O_{19}$ electrons are used so that they cannot contribute to the overall magnetization of the composite. As a result, low M_s values, as observed in Fig. 5b, can be obtained.

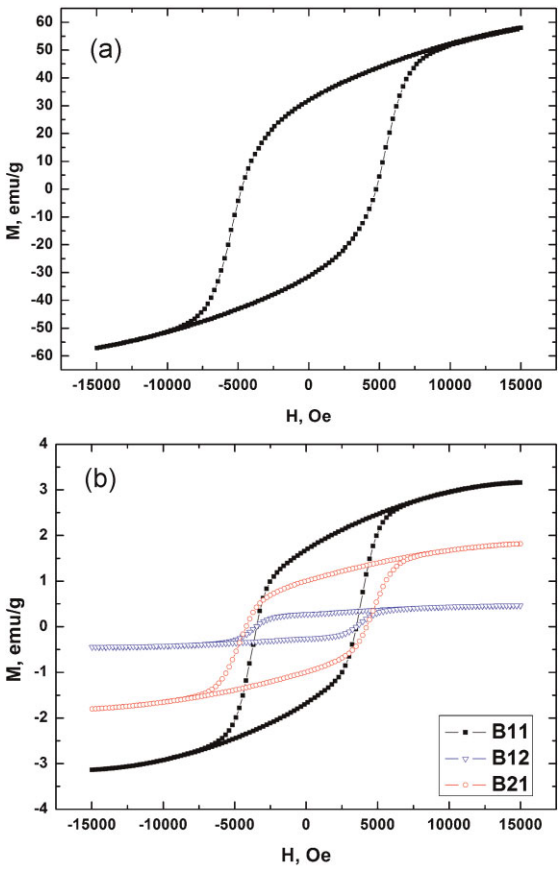

Figure 5 (online color at: www.pss-a.com) *M*–*H* hysteresis curves of (a) Ba-hexaferrite, (b) $BaFe_{12}O_{19}$–TiO_2–PPy nanocomposite with different weight fractions.

3.6 Microwave dielectric and magnetic properties The complex scattering parameters were obtained by microwave transmission and reflection measurements, and then, these parameters were analyzed by an Nicholson–Ross–Weir (NRW) algorithm with the physical dimensions and conditions [31–34]. To overcome the infinite number of roots of the complex transmission coefficient, the group delay method was used to compare measured and theoretical group delays. Thus, correct roots were chosen. The resultant dielectric complex permittivity $\varepsilon_r = \varepsilon'_r - j\varepsilon'_r$ and magnetic permeability $\mu_r = \mu'_r - j\mu''_r$ were calculated. The frequency dependency of real part of the permittivity, ε'_r, and dielectric loss factor, $\tan(\delta_e) = \varepsilon''_r/\varepsilon_r$, of all the samples are shown in Fig. 6a and b. The permittivity constant slightly decreases from 2 to 1.5 and 3.7 to 2.3 in the 8.2–18 GHz frequency range for the uncoated and PPy coated samples, respectively. As is clearly seen, the permittivity constant is almost doubled in composites coated with PPy polymer, (Fig. 6a). This means that the amount of polarization in the material increases with PPy coating. In PPy, there is a strong polarization due to the polaron/bipolaron and other bound charges that leads to a high value of ε'_r. Similarly, dielectric loss factors of PPy-coated composites are greater compared to the uncoated ones. Therefore, a PPy layer enhances the dielectric absorption in the composites. As frequency increases, these dipoles cannot reorient themselves along with the electric field, and thus, the dielectric constant decreases. The same observation has also been reported in PANI/BaM composites by Ting and Wu [35].The increase in dielectric loss by PPy coating results in an increase of the conductivity by means of the strong relationship between the conduction mechanism and the polarization mechanism (dielectric constant ε''_r), see Fig. 6b [36]. The conduction mechanism in ferrites is mainly based on charge hopping between Fe^{3+} and Fe^{2+} ions, and in the case of composites, charge transfer between NPs of BaM–TiO_2 and PPy chains can occur. This interaction between the BaM–TiO_2 surfaces and PANI layer may increase the conductivity on the BaM surface. Therefore, we may expect the shift in the resonance frequency [37], as observed in our samples B11 and B21 (Fig. 8). The greatest dielectric loss factor is observed in the sample B11 and other composites with PPy layer, B12 and B21, have nearly the same lossy characteristics.

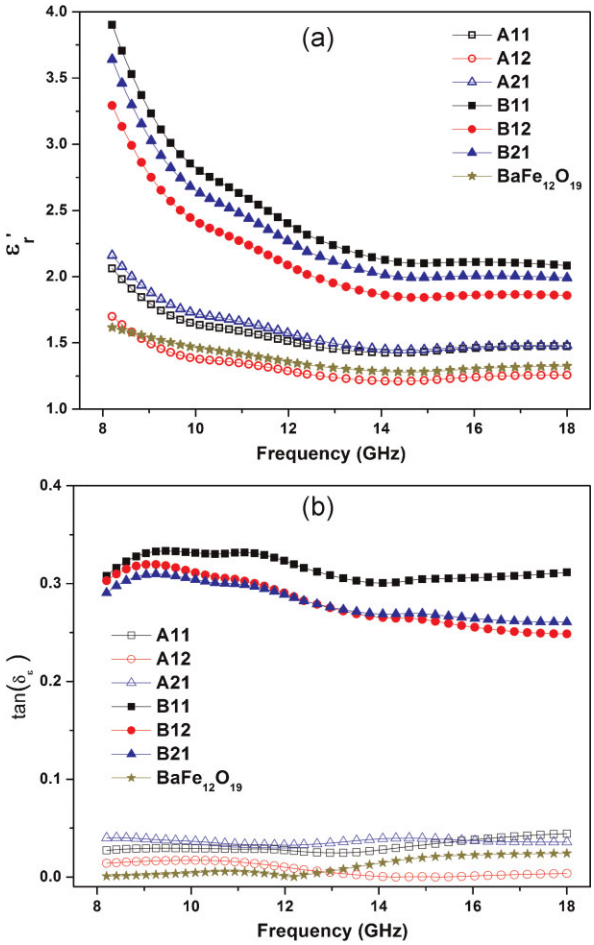

Figure 6 (online color at: www.pss-a.com) (a) The frequency-dependent real component of complex dielectric permittivity for all samples. (b) The frequency dependence of dielectric loss factor for all samples.

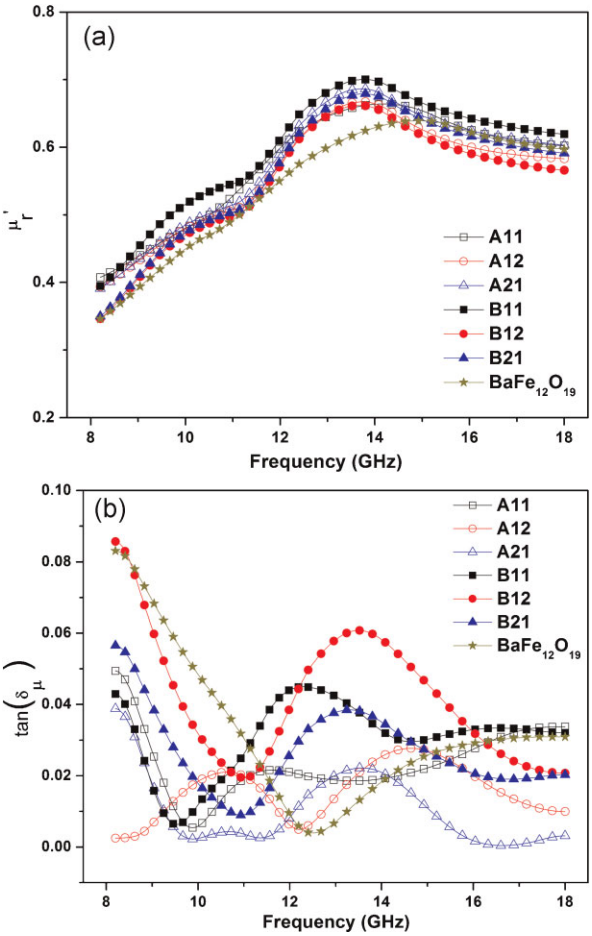

Figure 7 (online color at: www.pss-a.com) The frequency-dependent real component of complex magnetic permeability (a) and magnetic tangent loss (b) for all samples.

Figure 7 shows the real part of magnetic complex permeability, ε_r', and magnetic loss factor, $\tan(\delta_m) = \mu_r'' - \mu_r$. The μ_r of the BaM sample and that of others are almost the same. It seems that a dielectric filler, TiO_2, and a conducting polymer layer have no effect on permeability. There are similar results in the literature that report nearly the same permeabilities for the samples having different magnetic weight ratios [38, 39].

The magnetic loss factors are also of the same order with small differences in the wavy characteristic. The strength of magnetic loss of samples is weak compared to that of the dielectric loss. The magnetic loss tangents of all samples first decrease with frequency and have a narrow sink around 10–12 GHz, and then, increase at higher frequencies. Near the end of the Ku-band another decrease follows. Similar fluctuating permeability and loss factors were reported by Hongying et al. [40]. All these are combined effects of spin waves and ferromagnetic resonance that occurred above 5 GHz in most of the ferrites.

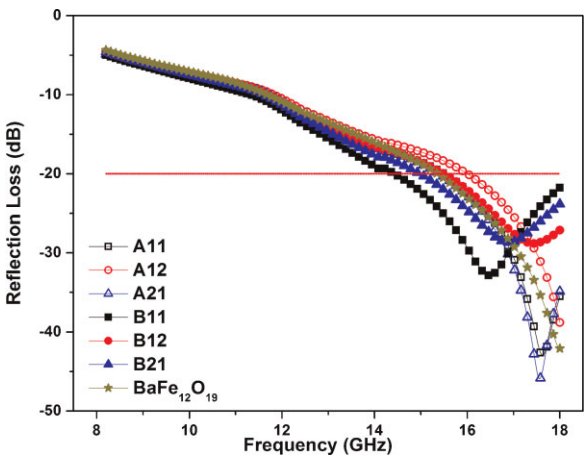

Figure 8 (online color at: www.pss-a.com) The frequency-dependent RL for all samples.

3.7 Reflection loss The RL calculation for metal backed microwave absorbing layer with normalized input impedance of Z_{in} is done by the relation

$$\mathrm{RL(dB)} = 20\log\left|\frac{Z_{in}-1}{Z_{in}+1}\right|,$$

where

$$Z_{in} = \sqrt{\frac{\mu_r}{\varepsilon_r}}\tanh\left[j\frac{2\pi fd}{c}\sqrt{\mu_r\varepsilon_r}\right].$$

Here, ε_r and μ_r are the complex permittivity and permeability of composites obtained from NRW algorithm, c the velocity of light, f the frequency of microwave, and d is the thickness of the composite sample ($d = 2$ mm). The frequency-dependent RL curves of BaM and all composites are shown in Fig. 8. Generally, the absorbers under investigation have a single RL peak at the end of the Ku band (16–18 GHz). The RL of absorbers in the X band are almost identical and decrease linearly with frequency. However, in the Ku band, RL behavior of the samples differs from each other significantly. It can be inferred that the PPy-coated composites have lower RL intensities than uncoated ones. Besides, the coated ones have wider absorption bandwidths. The relatively poor microwave absorption property displayed in PPy-coated samples could be related to the sharp decrease in magnetization values from $\sim 30\,\mathrm{emu\,g^{-1}}$ for the sample A11 to $\sim 3\,\mathrm{emu\,g^{-1}}$ for the coated one. It should be noted that the decrease in saturation magnetization corresponds to a decrease in the number of magnetic moments (*i.e.*, magnetic dipoles) which are used during the absorption of an EM wave. By increasing the weight fraction of BaM in uncoated composites RL increases and resonance frequency decreases. The highest RL of–45 dB was obtained with the sample A21 at around 17.5 GHz with 3 GHz bandwidth at −20 dB. Among the samples having a PPy layer, the best absorber appears to be B11 with an RL of nearly −35 dB that is centered at 16.5 GHz. This sample has a bandwidth of more than 4 GHz at −20 dB.

In the literature, it was reported that Mn–Co–Zr substituted Ba-ferrite has a resonance frequency between 16.75 and 19 GHz [41]. Similarly, in the Mn–Mg–Co–Ti-substituted BaM samples absorption occurs in the 16–17 GHz range with a maximum RL of −40 dB [14]. Our results are consistent with the above-mentioned studies. Finally, it should be noticed that the main absorption mechanism in our PPy-coated samples is due to the dielectric loss, as the dielectric tangent loss is greater than the magnetic tangent loss (Figs. 6b and 7b).

4 Conclusions Microwave absorbers including magnetic ($BaFe_{12}O_{19}$) and dielectric (TiO_2) fillers were synthesized with different $BaFe_{12}O_{19}$:TiO_2 weight fractions and coated with a conducting polymer, PPy. The microwave properties of BaM–TiO_2 nanocomposites with and without PPy coating were compared. It was shown that dielectric loss is enhanced significantly in the samples having a PPy layer in the whole frequency range (8–18 GHz). On the other hand, the magnetic loss of the all samples, *i.e.* coated and uncoated with PPy, first decreases and then increases with increasing frequency and have similar tendency. The RL values of all samples were centered at matching frequencies between 16 and 18 GHz. It can be concluded that uncoated composites absorb more energy compared to those with a PPy layer. However, absorption bandwidths seem to be wide in the PPy-coated composites. The sample, B11, with a PPy coating and having equal amount of magnetic and dielectric fillers showed the maximum RL of −35 dB at 16.5 GHz with approximately 4 GHz bandwidth at −20 dB. The matching frequencies of uncoated samples are very near to the end of the Ku band. The maximum RL obtained is −45 dB at 17.5 GHz with the sample having a higher amount of magnetic filler.

References

[1] F. Qin and C. Brosseau, J. Appl. Phys. **111**, 061301 (2012).
[2] G. Li, T. Xie, S. Yang, J. Jin, and J. Jiang, J. Phys. Chem. C **116**, (16), 9196 (2012).
[3] J. Zhou, J. He, G. Li, T. Wang, D. Sun, X. Ding, J. Zhao, and S. Wu, J. Phys. Chem. C **114**, 7611 (2010).
[4] A. Ghasemi, S. E. Shirsath, X. Liu, and A. Morisako, J. Appl. Phys. **111**(7), art. no. 07B543 (2012).
[5] M. Moniruzzaman and K. I. Winey, Macromolecules **39**, 5194 (2006).
[6] J. Liang, Y. Wang, Y. Huang, Y. Ma, Z. Liu, J. Cai, C. Zhang, H. Gao, and Y. Chen, Carbon **47**, 922 (2009).
[7] T. Kagotani, D. Fujiwara, S. Sugimoto, K. Inomata, and M. Homma, J. Magn. Magn. Mater. **272–276**, e1813 (2004).
[8] A. M. K. Eswai and M. M. Farag, Mater. Des. **28**, 2394 (2007).
[9] X. Chen, G. Wang, Y. Duan, and S. Liu, J. Phys. D: Appl. Phys. **40**, 1827 (2007).
[10] W. Chen, J. Zheng, and Y. Li, J. Alloys Compd. **513**, 420 (2012).
[11] J. Cao, W. Fu, H. Yang, Q. Yu, Y. Zhang, S. Liu, P. Sun, X. Zhou, Y. Leng, S. Wang, B. Liu, and G. Zou, J. Phys. Chem. B **113**, 4642 (2009).
[12] P. Saini, V. Choudhary, K. N. Sood, and S. K. Dhawan, J. Appl. Polym. Sci. **113**, 3146 (2009).
[13] J. L. Snoek, Physica **14**, 207 (1948).
[14] M. K. Tehrani, A. Ghasemi, M. Moradi, and R. S. Alam, J. Alloys Compd. **509**, 8398 (2011).
[15] A. Ghasemi, J. Magn. Magn. Mater. **324**, 1080 (2012).
[16] G. T. Rado, Rev. Mod. Phys. **25**, 81 (1953).
[17] T. Nakamura, T. Tsutaoka, and H. Hatakeyama, J. Magn. Magn. Mater. **138**, 319 (1995).
[18] P. Chandrasekhar, Conducting Polymers, Fundamentals and Applications: A Practical Approach, 1st ed. (Kluwer Academic Publishers, London, 1999).
[19] L. Olmedo, P. Hourquebie, and F. Jousse, Handbook of Organic Conductive Molecules and Polymers, edited by H. S. Nalwa (John Wiley and Sons Ltd., Chichester, 1997).
[20] Z. F. He, Y. Fang, X. J. Wang, and H. Pang, Synth. Met. **161**, 420 (2011).
[21] S. W. Phang, M. Tadokoro, J. Watanabe, and N. Kuramoto, Polym. Adv. Technol. **20**, 550 (2009).

[22] L. Du, Y. Du, Y. Li, J. Wang, C. Wang, X. Wang, P. Xu, and X. Han, J. Phys. Chem. C **114**, 19600 (2010).
[23] C. C. Yang, Y. J. Gung, C. C. Shih, W. C. Hung, and K. H. Wu, J. Magn. Magn. Mater. **323**, 933 (2011).
[24] O. Akman, H. Kavas, A. Baykal, M. S. Toprak, A. Coruh, and B. Aktas, accepted in: J. Magn. Magn. Mater., DOI: http://dx.doi.org/10.1016/j.jmmm.2012.09.032.
[25] T. Wejrzanowski, R. Pielaszek, A. Opaliniska, H. Matysiak, W. Lojkowski, and K. J. Kurzydlowski, Appl. Surf. Sci. **253**, 204 (2006).
[26] C. Kittel, Rev. Mod. Phys. **21**, 541 (1949).
[27] K. Majid, R. Tabassum, A. F. Shah, S. Ahmad, and M. L. Singla, J. Mater. Sci.: Mater. Electron. **20**, 958 (2009).
[28] B. Birsöz, A. Baykal, H. Sözeri, and M. S. Toprak, J. Alloys Compd. **493**, 481 (2010).
[29] H. Sözeri, Z. Durmuş, A. Baykal, and E. Uysal, Mater. Sci. Eng. B **177**(12), 949–955 (2012).
[30] Z. Durmus, B. Unal, M. S. Toprak, H. Sozeri, and A. Baykal, Polyhedron **30**, 1349 (2011).
[31] W. B. Weir, Proc. IEEE **62**, 33 (1974).
[32] A. M. Nicolson and G. F. Ross, IEEE Trans. Instrum. Meas. **19**, 377 (1970).
[33] J. Baker-Jarvis, E. J. Vanzura, and W. A. Kissick, IEEE Trans. Microw. Theory **38**, 1096 (1990).
[34] J. R. Baker-Jarvis, M. D. Janezic, J. H. Grosvenor, Jr., and R. G. Geyer, Transmission/Reflection and Short-circuit Line Methods for Measuring Permittivity and Permeability, NIST Technical Note 1355 (revised) (National Institute of Standards and Technology, Boulder, CO. 1993).
[35] T. Ting and K.-H. Wu, J. Magn. Magn. Mater. **322**, 2160 (2010).
[36] K. Iwauchi, Jpn. J. Appl. Phys. **10**, 1520 (1971).
[37] W. L. Bongiani, J. Appl. Phys. **43**, 2541 (1972).
[38] A. N. Yusoff and M. H. Abdullah, J. Magn. Magn. Mater. **269**, 271 (2004).
[39] A. Ohlan, K. Singh, A. Chandra, V. N. Singh, and S. K. Dhawan, J. Appl. Phys. **106**, 044305 (2009).
[40] L. Hongying, Z. Haifeng, Y. Lanying, X. Jijing, G. Shucai, M. Jian, and H. Guangyan, J. Rare Earths **25**, 590 (2007).
[41] A. Ghasemi and A. Morisako, J. Alloys Compd. **456**, 485 (2008).